BGO as a hybrid scintillator / Cherenkov radiator for cost-effective time-of-flight PET

Brunner, S. E.; Schaart, D. R.

DOI
10.1088/1361-6560/aa6a49

Publication date
2017

Document Version
Final published version

Published in
Physics in Medicine and Biology

OPEN ACCESS
IOP Publishing | Institute of Physics and Engineering in Medicine Physics in Medicine & Biology
Phys. Med. Biol. **62** (2017) 4421–4439 https://doi.org/10.1088/1361-6560/aa6a49

BGO as a hybrid scintillator / Cherenkov radiator for cost-effective time-of-flight PET

S E Brunner and D R Schaart

Radiation Science and Technology, Delft University of Technology, Mekelweg 15, 2629JB Delft, Netherlands

E-mail: s.e.k.brunner@tudelft.nl

Received 20 January 2017, revised 24 March 2017
Accepted for publication 30 March 2017
Published 5 May 2017

Abstract

Due to detector developments in the last decade, the time-of-flight (TOF) method is now commonly used to improve the quality of positron emission tomography (PET) images. Clinical TOF-PET systems based on L(Y)SO:Ce crystals and silicon photomultipliers (SiPMs) with coincidence resolving times (CRT) between 325 ps and 400 ps FWHM have recently been developed. Before the introduction of L(Y)SO:Ce, BGO was used in many PET systems. In addition to a lower price, BGO offers a superior attenuation coefficient and a higher photoelectric fraction than L(Y)SO:Ce. However, BGO is generally considered an inferior TOF-PET scintillator. In recent years, TOF-PET detectors based on the Cherenkov effect have been proposed. However, the low Cherenkov photon yield in the order of ~10 photons per event complicates energy discrimination–a severe disadvantage in clinical PET. The optical characteristics of BGO, in particular its high transparency down to 310 nm and its high refractive index of ~2.15, are expected to make it a good Cherenkov radiator. Here, we study the feasibility of combining event timing based on Cherenkov emission with energy discrimination based on scintillation in BGO, as a potential approach towards a cost-effective TOF-PET detector. Rise time measurements were performed using a time-correlated single photon counting (TCSPC) setup implemented on a digital photon counter (DPC) array, revealing a prompt luminescent component likely to be due to Cherenkov emission. Coincidence timing measurements were performed using BGO crystals with a cross-section of 3 mm × 3 mm and five different lengths between 3 mm and 20 mm, coupled to DPC arrays. Non-Gaussian coincidence spectra with a FWHM of 200 ps were obtained with the 27 mm^3 BGO cubes, while FWHM values as good as 330 ps were achieved

with the 20 mm long crystals. The FWHM value was found to improve with decreasing temperature, while the FWTM value showed the opposite trend.

Keywords: positron emission tomography, PET, time-of-flight, TOF, BGO, silicon photomultiplier, SiPM

(Some figures may appear in colour only in the online journal)

1. Introduction

Due to detector developments in the last decade, the time-of-flight (TOF) method is now realizing its potential for improving the quality of positron emission tomography (PET) images. The TOF method improves the statistical properties of the data by reducing ambiguity (i.e. noise), leading to a better signal-to-noise ratio (SNR). The benefit of using TOF information in PET has been addressed by various research groups (Moses 2007, Karp *et al* 2008, Conti 2011, Vandenberghe *et al* 2016).

Commercial vendors have recently developed whole-body clinical TOF-PET systems based on L(Y)SO:Ce crystals read out with silicon photomultipliers (SiPMs), which offer coincidence resolving times (CRT) between 325 ps FWHM and 400 ps FWHM (Miller *et al* 2015, Grant *et al* 2016, Miller 2016). Moreover, demonstrator systems equipped with clinical detectors have been built, achieving CRT between 200 ps FWHM and 250 ps FWHM (Schug *et al* 2015, Borghi *et al* 2016). Even better CRT, well below 100 ps FWHM, have been achieved in laboratory (Schaart *et al* 2010, Nemallapudi *et al* 2015, Cates and Levin 2016, Gundacker *et al* 2016b, Brunner *et al* 2016a, 2016b).

After the first growth of single crystals of bismuth germanate (i.e. bismuth germanium oxide, $Bi_4Ge_3O_{12}$, short: BGO) by Nitsche (Nitsche 1965), the material was introduced as a scintillator in PET systems in the late 1970s (Cho *et al* 1978, Thompson *et al* 1979, Derenzo *et al* 1981). At that time, it hardly seemed possible to apply the TOF-PET technique with BGO. Nevertheless, its very high stopping power and photo-electric fraction at 511 keV made BGO a preferable PET scintillator and research efforts in TOF-PET were halted in the late 1980s (Moszyński *et al* 1981, Conti 2011). In the 1990s, the attractive properties of cerium-doped Lu_2SiO_5 (LSO:Ce), in particular its high light yield and good attenuation coefficient, made it become the state-of-the-art scintillator in PET and triggered a revival of TOF-PET research after the year 2000 (Melcher and Schweitzer 1992, Surti *et al* 2007, Vandenberghe *et al* 2016). Nevertheless, BGO still provides, in addition to a considerably lower prize, a superior attenuation coefficient for annihilation quanta and a higher photoelectric fraction than L(Y)SO:Ce. It also has no intrinsic background-radiation. The scintillation properties of BGO and LSO:Ce are summarized and compared in table 1.

1.1. Cherenkov effect for TOF-PET

First proposed by Ooba *et al* (2004), Miyata *et al* (2006), the Cherenkov effect has gained increasing interest in the TOF-PET community in recent years. Several groups obtained CRTs between ~70 ps FWHM, using PbF_2 coupled to multi-channel plate photomultiplier tubes (MCP-PMTs), and ~300 ps FWHM, using the same material coupled to SiPMs (Dolenec *et al* 2010, Korpar *et al* 2011). Measurements with several Cherenkov emitters coupled to digital SiPMs (dSiPMs) resulted in CRTs of ~150 ps FWHM in coincidence with a scintillator (Brunner 2014). In parallel, several theoretical studies and simulations of Cherenkov-based

Table 1. Properties of BGO and LSO:Ce.

	$Bi_4Ge_3O_{12}$	Lu_2SiO_5:Ce
Light yield (photons × MeV^{-1})	8200[a], 9000[j]	30 000[j], 30 900[b],
Cherenkov yield for 511 keV (photons)	∼20 (305–750 nm)[k]	∼9 (390−750 nm)[k]
Rise time (ps)	30 ± 30[c]	69[d]
		30 ± 30 (88%), 350 (12%)[c]
Decay time (ns)	60 (10%), 300 (90%)[e]	40 − 43[d]
	85 (7%), 370 (93%)[g]	19 (8%), 38 (92%)[f]
	5.8 (1%), 24 (4%), long (95%)[c]	
Refractive index	2.39 (310 nm), 2.2 (420 nm)[h]	1.827 (420 nm)[b]
Density (g × cm^{-3})	7.13[i]	7.4[j]
Electron density Z_{eff}	75[i]	66[i]
Absorption length 511 keV (mm)	10.4[j]	11.4[j]
Fraction photoelectric effect at 511 keV	0.4[j]	0.32[j]
Intrinsic background radiation	no	yes

[a] Holl *et al* (1988).
[b] Spurrier *et al* (2008).
[c] Derenzo *et al* (2000).
[d] Gundacker *et al* (2016b).
[e] Moszyński *et al* (1981).
[f] Weele *et al* (2015).
[g] Wolszczak *et al* (2014).
[h] Williams *et al* (1996).
[i] Lecoq *et al* (2006).
[j] Humm *et al* (2003).
[k] See text for details.

TOF-PET detectors have been published (Brunner *et al* 2013, 2014, Derenzo *et al* 2014, Somlai-Schweiger and Ziegler 2015).

Compared to scintillation, Cherenkov emission can be considered instantaneous (to within a few ps). Cherenkov photons are emitted by the hot electrons created upon the absorption of 511 keV gamma photons in the detector material. The Cherenkov photon yield, N, can be estimated using the Frank–Tamm equation

$$\frac{\mathrm{d}N^2}{\mathrm{d}x\mathrm{d}\lambda} = \frac{2\pi\alpha}{\lambda^2}\left(1 - \frac{1}{n(\lambda)^2\beta^2}\right), \tag{1}$$

where x denotes the electron path length, λ the wavelength of the emitted photons, n the refractive index of the material, and $\beta = v_p/c$ the phase velocity of the electron in terms of the speed of light in vacuum. In general the emission yield per unit path length is approximately proportional to $1/\lambda^2$ (Jelley 1958).

Desired characteristics of a Cherenkov radiator thus include a high transparency over a wide range of wavelengths, especially towards the ultraviolet (UV) region, and a high refractive index. Nevertheless, the Cherenkov photon yield is expected to be rather low, typically about ∼10 to ∼30 photons per 511 keV photon in good Cherenkov radiators. This makes Cherenkov emission very challenging to exploit in PET: on the one hand, energy determination and, therefore, discrimination of Compton-scattered events becomes almost impossible while, on the other hand, the overall time resolution becomes highly dependent on the single-photon time resolution (SPTR) of the photosensor.

A strategy for energy discrimination based on the refractive index of the material was proposed and investigated by Ooba *et al* (2004) and Korpar *et al* (2011). Bilevych *et al* suggested

that the development of photosensors with extremely good SPTR as well as PDE might facilitate the realization of TOF-PET detectors based on pure Cherenkov radiators in future (Bilevych *et al* 2016). As another potential solution, Brunner *et al* proposed to combine event timing based on Cherenkov emission with energy discrimination based on scintillation in a hybrid scintillator/Cherenkov radiator (Brunner *et al* 2014, Brunner 2014).

A first experimental study on hybrid Cherenkov/scintillation detection in Ce-doped LuAG ($Lu_3Al_5O_{12}$:Ce) crystals led to the conclusion that Cherenkov photons were unlikely to be detected, as most of them are absorbed by the Ce^{3+} ions in this material (Brunner 2014). Nevertheless, investigations were continued using Monte Carlo simulations, revealing BGO as a highly promising candidate for a hybrid scintillator/Cherenkov radiator for PET (Brunner *et al* 2013, 2014). These considerations were experimentally verified in a proof-of-concept measurement performed with two 3 mm × 3 mm × 8 mm BGO crystals coupled to dSiPMs. A CRT of 300 ps FWHM was found for the faster one of the two components observed in the time difference spectrum (Brunner *et al* 2014, Brunner 2014). Another study with BGO was later presented by Kwon *et al* (2016), who compared UV-sensitive and RGB-sensitive analog SiPMs for two different crystal sizes. In that work, time resolutions of 267 ps FWHM and 562 ps FWHM were reported for 2 mm × 2 mm × 3 mm and 3 mm × 3 mm × 20 mm BGO crystals, respectively, when applying Lorentzian fitting functions.

This work investigates the practical potential of BGO as a cost-effective, hybrid scintillator / Cherenkov radiator for TOF-PET. A systematic study on the time resolution of BGO crystal rods with different lengths is performed. As the time jitter introduced by photon propagation is significant in such rods, results on very short crystals (3 mm) should approach the best achievable time resolution, whereas results on longer rods (20 mm) should demonstrate the time resolution of crystals with high detection efficiency useful for TOF-PET systems. Simultaneously, the energy resolution was determined to investigate the feasibility of the hybrid detector approach. The measurements were performed at different temperatures to study the influence on the time resolution of the temperature dependence of the SiPM dark count rate and the scintillation time constants. It is noted that we refer to the observed fast luminescent component as Cherenkov emission: (1) for simplicity, (2) since it is plausible, and (3) because we have found no evidence to the contrary. Nevertheless, we cannot rule out the possibility that other fast luminescent mechanisms may also play a role.

2. Material and methods

Equation (2) was used to calculate an average number of emitted Cherenkov photons for BGO and LSO:Ce given in table 1. For BGO the Cherenkov photon emission was calculated within the wavelength region between 305 nm and 750 nm using the refractive index from Williams *et al* (1996), an average electron energy of 300 keV, an energy range of 60 keV to 450 keV and an average electron range of 350 μm (Berger *et al* 2005). For LSO:Ce the number of emitted Cherenkov photons was calculated between 390 nm and 750 nm according to the LSO:Ce transmittance. The refractive index measured by Jellison *et al* (2012) and an average electron range of 315 μm was used (Berger *et al* 2005). The results are included in table 1.

Three types of experiments were performed on BGO: measurements of the optical properties (i.e. transmittance and emission spectra), the rise time, and the coincidence timing performance. All measurements (except for the emission measurement) were performed in a temperature-controlled environment.

The $Bi_4Ge_3O_{12}$ crystals investigated were produced by PJT Elect[1] and had a cross-section of 3 mm × 3 mm. Five different crystal lengths were investigated: 3 mm, 5 mm, 8 mm, 12 mm, and 20 mm. All crystal surfaces were optically polished. Unless otherwise noted, one of the 3 mm × 3 mm crystal surfaces was coupled to the photosensor, using BC-630 optical grease from Saint-Gobain. All other surfaces of the crystal were wrapped in about 10 layers of Teflon tape (0.075 mm thick RS thread seal tape).

Given the relatively low number of Cherenkov photons expected per event, the Philips digital photon counter (DPC) was chosen as the photosensor in all experiments. This digital silicon photomultiplier (dSiPM) array allows triggering on the first detected photon (Brunner *et al* 2014, Gundacker *et al* 2016b). Additionally, the DPC array provides a validation cycle that can be used to reject unwanted triggers resulting from dark counts. The DPC array consists of 16 independent DPC chips also called dies, arranged on a so-called tile of 32 mm × 32 mm (Frach *et al* 2009, Schaart *et al* 2015). Each die is sub-divided into 4 pixels, each of which comprises 3200 single-photon avalanche diodes (SPADs). A schematic drawing of the layout is shown in figure 1.

An interesting feature of the Philips DPC is the possibility to address individual SPADs and activate or deactivate them. This feature can be used to determine the dark-count rate (DCR) of each individual SPAD and deactivate the cells with the highest rates, or, as proposed here, to activate only a single SPAD so as to use the sensor for time-correlated single-photon counting (TCSPC) measurements.

2.1. Transmittance

The transmittance of the BGO samples was studied using a commercial setup from Avantes consisting of a combined Halogen/Neon lamp (model AvaLight-DHc) and a spectrometer (model AvaSpec-3648). A BGO rod with 3 mm thickness was placed in a UV transmitting cuvette-holder (Plastibrand, semi-micro UV-cuvette), which was connected to the lamp and the spectrometer using optical fibers.

2.2. X-ray excited emission spectrum

A cube of BGO with edge lengths of 3 mm was exposed to continuous x-ray radiation at a voltage of 35 kV and an anode current of 10 mA. The corresponding emission spectrum was measured using a PMT (Hamamatsu R943-02), after the scintillation light had passed a Czerny–Turner monochromator (Action Motion Corporation, model vm504) with a spectral resolution $<$2 nm.

2.3. Rise time

A simple setup for time-correlated single-photon counting was realized for measuring the intrinsic rise-time (and other time constants) of the BGO luminescent emission upon excitation by 511 keV photons (Bollinger and Thomas 1961). This setup was inspired by the approach proposed by Seifert *et al* (2012). However, in this work the 48 ps FWHM single-photon time resolution of the individual SPADs of the Philips DPC was exploited (Brunner *et al* 2016b).

Figure 3 shows a schematic drawing of the TCSPC setup implemented on a single DPC. A fast Ca-codoped LSO:Ce crystal was coupled to the DPC, acting as reference scintillator (*start*). It was operated normally with a full DPC pixel activated below the crystal (only the

[1] Shanghai Project Electronic Technology Co., Ltd., China

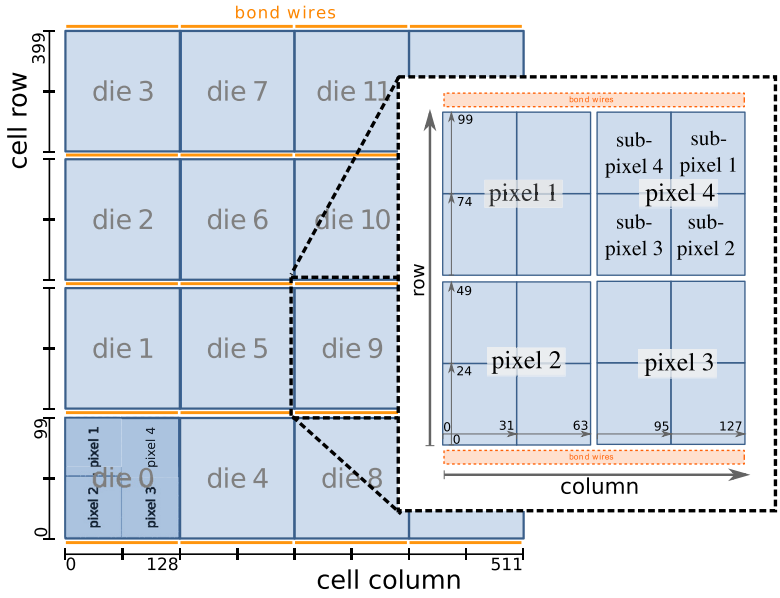

Figure 1. Schematic layout of the Philips digital photon counter. Cell column and cell row address the individual SPADs. Picture taken from the Philips Digital Photon Counting (DPC) manual. Reproduced with permission from Schulze (2015).

5% of the 3200 SPADs with the highest DCR were deactivated). The scintillator under test was mounted in line with the reference crystal and a ^{22}Na source in between them. The rise-time of the scintillator can be determined in TCSPC-mode by activating only a single SPAD of the DPC below the crystal under test (*stop*). Only one SPAD was chosen as each SPAD is connected to the TDC with an electrical line of different length, so additional jitter would be added if multiple SPADs were used, see (Frach 2012, Liu *et al* 2016, Brunner *et al* 2016b). All measurements were done in a temperature-controlled environment.

As the DCR of the stop-SPAD can influence the results, a SPAD with a low DCR was selected by using the feature of determining the DCR for each individual SPAD, i.e. dark count mapping (Frach *et al* 2010). To avoid border effects due to reflections, the SPAD was also required to be located within the central area of the pixel. The SPAD finally chosen as the stop-detector had a DCR $<$5 cps at 20 °C.

For determining the intrinsic response of BGO to the absorption of a 511 keV annihilation photon, the influence of internal reflection of optical photons was further minimized by black-taping the crystal. To reject Compton-scattered annihilation photons, the BGO crystal under test (3 mm $\times$ 3 mm $\times$ 5 mm) was positioned such that it partly covered a pixel of a neighboring die (see figure 3). The photons arriving on this pixel were counted and used for energy discrimination. To improve the detection efficiency of this part of the sensor, the light was spread over the whole pixel using a light-guide made of optical glue (Cargille Meltmount 1.582), which additionally had the function of holding the crystal in position. The part of the crystal covering the stop-SPAD was coupled using UV-transmitting optical grease (BC-630 by Saint Gobain). It should be noted that the start detector, the stop-SPAD, and the energy-recording pixel were each placed on a different die, because a die is the smallest independent unit of a DPC sensor and each die can provide only a single timestamp. Moreover, it is to be noted that a die is only quasi-independent, as the trigger and validation thresholds as well as the validation- and integration lengths can only be set for the whole tile.

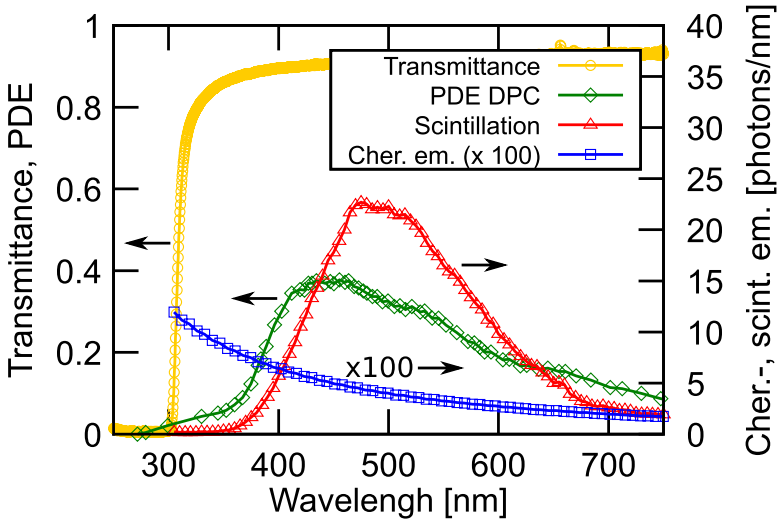

Figure 2. Yellow circles: transmission spectrum of a 3 mm thick BGO sample (not corrected for reflection); green diamonds: PDE of the DPC (Philips Digital Photon Counting, Aachen, Germany 2015); red triangles: emission spectrum of BGO cubes with 3 mm edge lengths upon x-ray excitation (normalized to a total number of ∼4100 emitted photons); blue squares: calculated Cherenkov emission yield (normalized to a total number of ∼20 emitted photons and multiplied by a factor of 100 for better visibility).

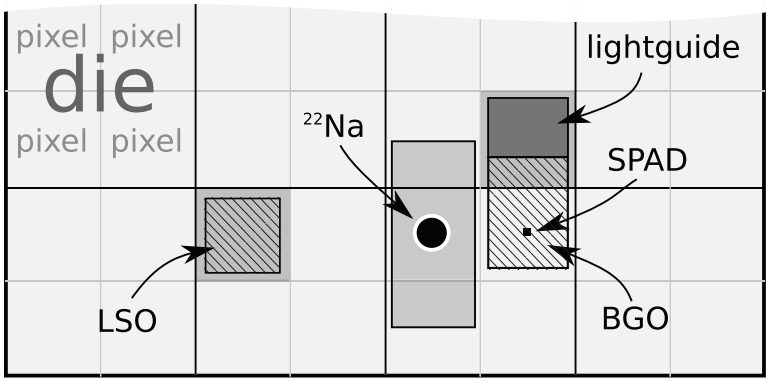

Figure 3. Schematic drawing of the TCSPC setup based on a single DPC tile. Drawn are 8 out 16 dies of a DPC-sensor tile. See text for explanation.

The trigger threshold was set to 1 for all measurements, resulting in a time-pickoff on the first detected photon. This was done to achieve the best time resolution as well as be able to record events from the stop-SPAD. The validation scheme for the whole DPC array was set to 4 (corresponding to a statistical validation threshold of about 17 fired SPADs) in order to reduce the amount of recorded data, see Tabacchini *et al* (2014). Since events on the stop-SPAD could not be validated with this validation scheme, neighbor logic was used instead. That is, when either the start detector or the energy-discriminating pixel registered a valid event, simultaneous events on the other two detectors were validated. As the maximum possible validation interval for the DPC is 40 ns, this strategy for data reduction can only be

applied for TCSPC of the first 40 ns of the luminescence response of the crystal under test. To decrease the amount of data even further, the coincidence sorting function was used to on-the-fly delete all events not being triple coincidences within a coincidence window of 20 ns.

It is known that the validity of the luminescence response measured with the TCSPC method is dependent on the mean number of photons arriving at the stop-detector per registered 511 keV event, which should be $\ll 1$ (Seifert *et al* 2012). The value was cross-checked in a separate measurement where 90% of the SPADs of the same pixel as the stop-SPAD were activated (i.e. 2880 SPADs). The number of detected photons per 511 keV photoelectric interaction was found to be around 235 photons. Dividing by the number of active SPADs leads to a probability of photon detection of $\cong 0.08$.

An estimation of the impulse response function (IRF) of the TCSPC setup was done using a high-effective-Z, high-refractive-index Cherenkov radiator as stop crystal. Specifically, an undoped LuAG crystal with a size of 3 mm × 3 mm × 8 mm was used. It was reported that pure LuAG shows mainly Cherenkov emission upon excitation of 511 keV annihilation photons and thus is a good candidate to estimate the IRF including the photon travel time spread within the crystal (Lecoq *et al* 2010, Brunner 2014, Gundacker *et al* 2016b). The crystal was black-taped and coupled to the SPAD with optical grease (BC-630) and to the stop-pixel with Cargille Meltmount 1.528, in the same way as the BGO crystals under test (see figure 3). The measurement showed a normally distributed IRF with a $\sigma = 50.15$ ps $\pm$ 1.6 ps. This result is used to correct the measured data, so as to obtain the intrinsic time profile of the luminescent emission within the crystal under test. A detailed description of for determination of the IRF is being prepared for submission in a separate publication.

The data is assumed to comprise one or more scintillation components, each fitted with a double exponential luminescence response function, p_{t_e}, described by an intensity ρ, an interaction time θ, a rise time, τ_r, and a decay time τ_d. The Cherenkov response is described as a delta function, δ_C,

$$p_{t_e}(t|\theta) = \sum_{i=1}^{N} \frac{\rho_i}{\tau_{d,i} - \tau_{r,i}} \left(e^{-\frac{t-\theta}{\tau_{d,i}}} - e^{-\frac{t-\theta}{\tau_{r,i}}} \right) \cdot \Theta(t-\theta) + \delta_C(t-\theta), \tag{2}$$

with Θ the Heaviside step function and N the number of independent luminescence response channels. Before fitting, this function is convolved with the Gaussian shaped IRF as described in Seifert *et al* (2012) and Gundacker *et al* (2016b).

2.4. Coincidence timing

Timing studies were done using a basic coincidence setup, in which two BGO crystals of equal dimensions were mounted for each measurement. The cross-section of all crystals was 3 mm × 3 mm, while 5 different crystal lengths were investigated, i.e. 3 mm, 5 mm, 8 mm, 12 mm, and 20 mm. Figure 4 shows a photograph of the crystals tested. Each of the crystals was wrapped on 5 sides with Teflon tape (0.075 mm thick RS thread seal tape). The remaining 3 mm × 3 mm surface was coupled to a DPC-pixel using optical grease (BC-630 by Saint Gobain). The coincidence setup was realized by arranging the two assembled detectors face-to-face at a distance of ∼5 cm and with a ^{22}Na source in between them. A balance between the influences of DCR and PDE was found by deactivating 5% of the most active SPAD. The trigger scheme was set to 1, resulting in a time-pickoff of the first detected photon. Furthermore, the validation scheme was set to 4 and a validation interval of 10 ns was chosen. In this configuration, after 10 ns it is evaluated if in each of 4 logically connected segments of a DPC sub-pixel a SPAD was fired. On average 17 photons need to be detected within 10 ns to have

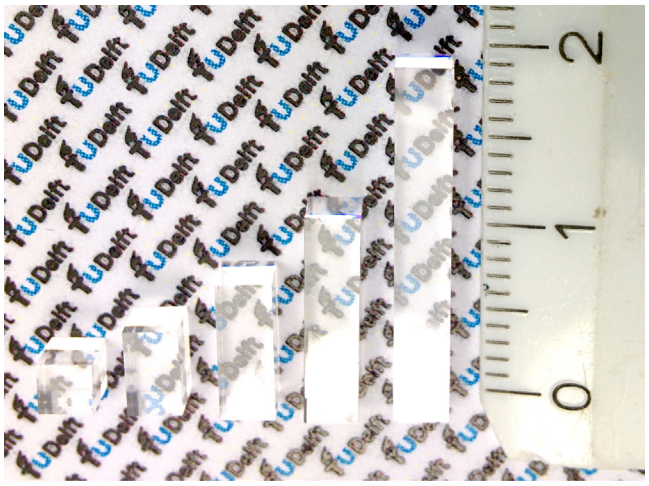

Figure 4. Photograph of the BGO samples tested in this work. All crystals have a cross-section of 3 mm × 3 mm. From left to right, the crystal lengths are 3 mm, 5 mm, 8 mm, 12 mm, and 20 mm.

the event validated in this scheme. The integration interval for detecting photons following the validation was chosen to be 1285 ns (∼4 × the decay time of BGO). A detailed description about the trigger and validation functionality and theory can be found in Frach *et al* (2010), Tabacchini *et al* (2014) and Schulze (2015). The influence of the DCR and light yield on the time resolution was investigated by repeating the measurements at different temperatures, viz. −31 °C, −20 °C, 0 °C, and 20 °C.

In addition to the coincidence timing performance, the energy resolution was investigated by fitting the full-energy peak with a Gaussian function and deriving the mean number of detected photons μ_{phot} and the standard deviation σ_{phot} from the fit. The energy resolution was calculated as $E_{\text{res}} = \Delta E_{\text{FWHM}}/E = 2.35 \times \sigma_{\text{phot}}/\mu_{\text{phot}}$. The results of the same fits were used for event selection in the analysis of the coincidence timing results, using an energy window ranging from $\mu_{\text{phot}} - \sigma_{\text{phot}}$ up to $\mu_{\text{phot}} + 2 \times \sigma_{\text{phot}}$.

The resulting time-difference histogram is expected to have a non-Gaussian distribution, as it is the result of multiple luminescent processes with different time constants. Therefore, both the FWHM and FWTM are used in this work to characterize the time-difference spectra. The binning of the histogram was done corresponding to the width of the TDC-bins of the DPC, i.e. 10 ns / 512 ≅ 19.5 ps. Furthermore, the data was smoothed by linear interpolation between the bin centers. The FHWM and the FWTM were derived from the interpolated data.

As the determination of the FWHM and FWTM from a histogram is sensitive to statistical fluctuations of the maximum of the histogram, a conservative error estimation was done using the Poissonian errors of the histogram frequencies, $\pm\sqrt{n_i}$, for $i = 1, 2, 3, ..., n_{\text{tot}}$. That is, for the upper error of the time resolution, the lower error of the histogram maximum ($n_{\text{max}} - \sqrt{n_{\text{max}}}$) was used and defined as the new maximum. Then, the FWHM and FWTM were determined using the upper errors of the corresponding histogram frequencies ($n_i + \sqrt{n_i}$). As described before, linear interpolation was done between the bin centers. This procedure was repeated to determine the lower errors of the FWHM and FWTM, this time using the upper error of the bin with the maximum number of counts and the lower errors for the other two bins.

The FWHM (or FWTM) is a convenient measure to summarize the shape of a probability distribution, but only characterizes it fully if the shape is known *a priori*, for example in

the case of a Gaussian time difference histogram. In the present study, we expect the measured timing spectrum to have a less trivial shape, as it is composed of multiple components. Therefore, we will use an additional way of describing the data, viz. the coincidence time window t_p within which a certain percentage p of the total number of coincident events occur. To this end, the cumulative frequency distribution (CFD) of the time-difference histogram is obtained first. Then, the CFD is compared to a threshold value p_{th} that is increased in steps of 5% and the time $t(p_{\text{th}})$ at which each threshold is reached is recorded. Finally, t_p is calculated as $t_p = t(p_{\text{th}} = 50 + \frac{p}{2}) - t(p_{\text{th}} = 50 - \frac{p}{2})$. For example, $t_{40\%}$ is calculated as the difference between the times at which the threshold values 30% and 70% are reached.

3. Results and discussion

3.1. Transmittance and x-ray excited emission spectrum

The yellow circles in figure 2 represent the transmission spectrum of a 3 mm thick BGO sample, measured as described in section 2.1 and corrected for the spectrometer dark spectrum and the lamp emission spectrum. The transmission of the sample exhibits a sharp cut-on of the transmission at about 310 nm and saturates above 90% at wavelengths above 400 nm. It is noted that the spectrum was not corrected for reflectivity.

The red triangles in figure 2 show the emission spectrum upon x-ray excitation of a 3 mm thick BGO sample. This spectrum was measured according to the description given in section 2.2 and has been corrected for the PMTs spectral sensitivity. Additionally, the spectrum has been normalized to a total number of 4100 photons, which is the expected light yield at 511 keV (Holl *et al* 1988).

In the same figure it can be seen that the transmittance of BGO is beneficial for letting the Cherenkov photons propagate through the material, down to wavelengths of ∼305 nm. As calculated in section 2 the expected Cherenkov yield equals about 20 emitted photons. When comparing the Cherenkov emission and the BGO transmission spectra with the PDE of the DPC, only a fraction of the emitted Cherenkov photons can be expected to be detected.

3.2. Rise time

Figure 5 shows the temporal luminescent response of BGO upon excitation by an annihilation photon, measured using the TCSPC method described in section 2.3. The data is plotted within a range of 2 ns, for a measurement temperature of 20 °C and a selected energy of 511 keV (within a range of $-1\sigma, +2\sigma$). The inlay shows the data for the first 20 ns, plotted on a logarithmic time scale. The measurement reveals a significant prompt component with a FWHM of about 160 ps, preceding slower luminescent components. This fast component cannot be explained by the scintillation characteristics found for BGO in literature (Moszyński *et al* 1981, Derenzo *et al* 2000, Humm *et al* 2003, Lecoq *et al* 2006), but agrees with the expected response due to Cherenkov emission according to Brunner *et al* (2014) and Brunner (2014). Hence, it is plausible that the observation is caused by the Cherenkov effect.

The data was fitted using a single scintillation rise time, two scintillation decay time components, an instantaneous (Cherenkov) component, and a normally distributed IRF with σ_{IRF} of 50.15 ps. The fit yielded a scintillation rise-time of 50.9 ps ± 48.8 ps, a fast decay component of 1.37 ns ± 0.4 ns (<1%) and a longer component of 62.9 ns ± 3.9 ns. The fitting range was limited to 20 ns due to instrumental constraints imposed by the neighbor logic of the DPC. It therefore has to be noted that the decay component of 62.6 ns could be influenced by the

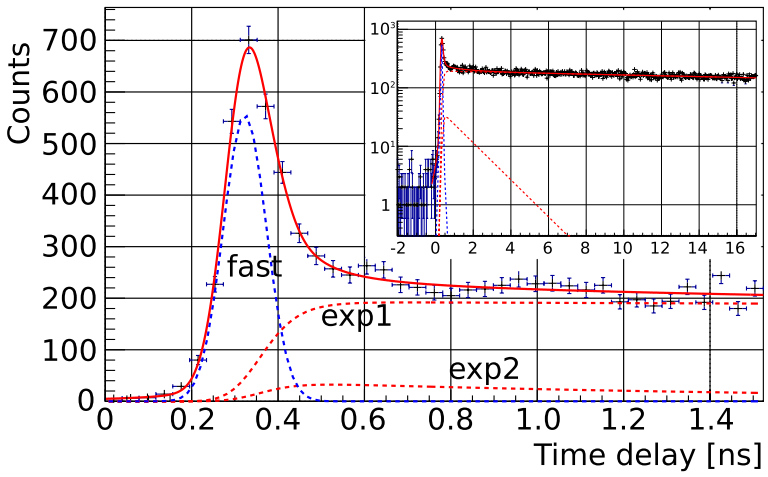

Figure 5. Luminescent response of BGO during the first 1.5 ns following excitation by 511 keV annihilation photons including a fit of the data comprising a delta function (fast), and two double-exponential functions (exp1 and exp2). The functions where convolved with a normally distributed IRF, see text for details. The inlay shows the response within the first 20 ns on a logarithmic time scale.

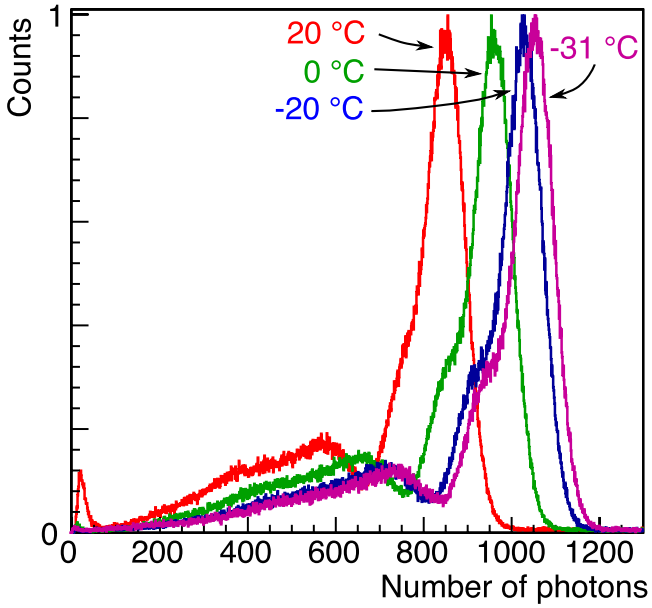

Figure 6. Normalized energy spectra of one of the two 3 mm × 3 mm × 3 mm BGO detectors measured in coincidence at 4 different temperatures.

short fitting range and should not be interpreted as the BGO intrinsic decay time, although the result agrees with the fast component of the BGO emission reported to be 60 ns and 300 ns (Moszyński *et al* 1981). Furthermore, the ∼1 ns decay component might be related to optical cross-talk caused by photon emission during avalanche breakdowns in the activated neighbouring DPC pixel used for energy discrimination.

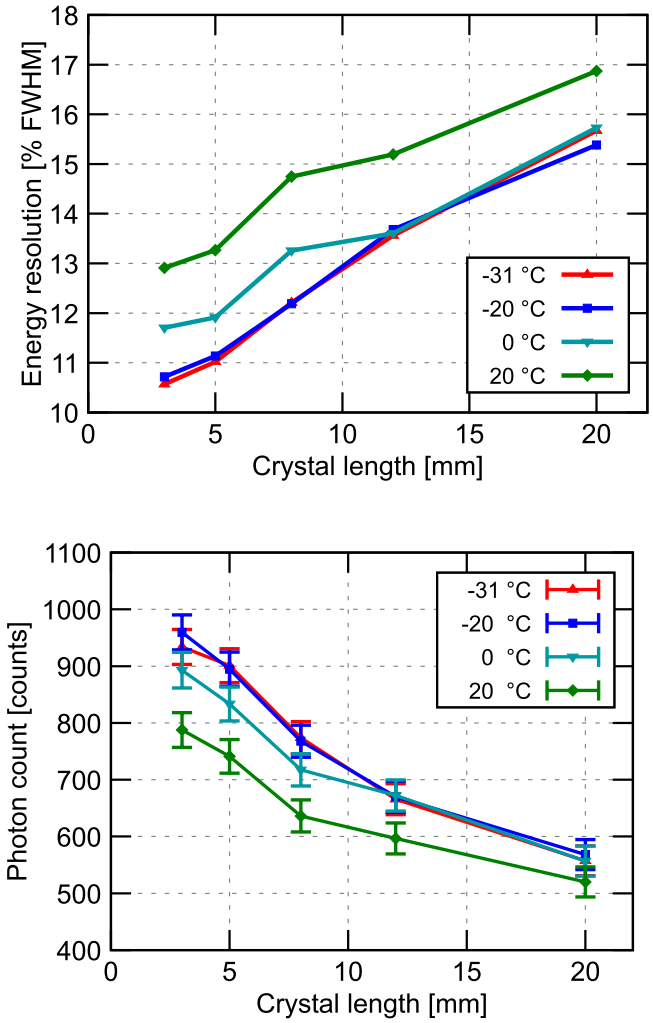

Figure 7. Energy resolution (top) and mean number of detected photons (bottom) of the BGO samples at 511 keV as a function of crystal length.

3.3. Coincidence timing

Figure 6 shows the number of photons detected per event for one of the two detectors in the coincidence setup described in section 2.4. The histograms of this figure were obtained from BGO cubes with side lengths of 3 mm at 4 different temperatures. Similar data were obtained for all crystals and used to determine the energy resolution and the mean number of photons detected per absorption of a 511 keV photon. The results are shown in figure 7. It should be noted that the values shown represent mean values calculated from both detectors in coincidence.

The data of figure 7 are plotted for 5 crystal lengths and 4 different temperatures. The energy resolution ranges from 10.6% FWHM at −31°C and 3 mm length up to 16.8% FWHM at 20°C and 20 mm length. At temperatures $\leqslant$ 0°C, only a small variation of the energy resolution with temperature is observed, especially for the larger crystals. The same is found for the number of detected photons. For the 12 mm and 20 mm crystals in particular, very similar

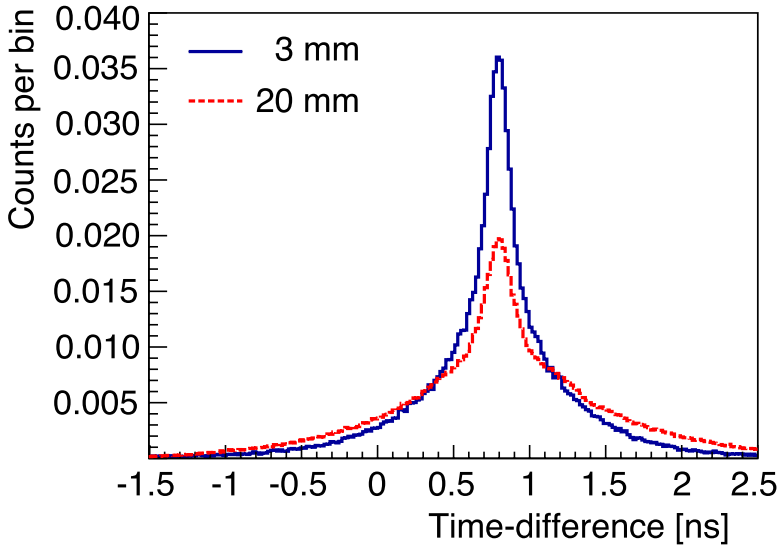

Figure 8. Normalized time-difference histograms of the 3 mm (blue solid curve) and 20 mm long (red dashed curve) BGO crystals measured in coincidence at 20°C.

numbers of photons are detected at temperatures between −31°C and 0°C. Correspondingly, their energy resolution remains essentially constant at these temperatures. However, when the temperature is increased to 20 °C, the number of detected photons reduces and the energy resolution worsens for all crystal lengths. In summary, both the number of detected photons and the energy resolution improve with decreasing crystal length and decreasing temperature. This behavior is expected and agrees with literature (Wolszczak 2014).

Figure 8 shows two examples of the time difference histograms obtained in the coincidence setup, viz. for the 3 mm BGO cubes (solid blue curve) and the 20 mm long BGO rods (dashed red curve). Figure 9 shows the FWHM (top) and FWTM (bottom) of the time difference spectra as a function of the crystal length at different temperatures. It can be seen that the FWHM improves towards shorter crystal lengths. This can be attributed to a decreasing influence of photon transport inside the crystal on one hand, and an increasing influence of Cherenkov photon emission on the other hand.

A variation with temperature is also observed; the best FWHM values occur at the lowest temperatures. This can be explained by the decreasing DCR of the DPC, which is reduced by 50% each time the temperature is decreased by about 7 °C. The observation that the FWHM appears to show a maximum at a crystal length of 12 mm for temperatures below 20 °C was investigated further. Additional measurements were performed with another pair of BGO crystals from the same producer, the same size and the same surface polishing but cut from a different boule. For these crystals a higher number of photons of up to +20% and an improvement of the energy resolution of up to 15% was observed. The time resolution (FWHM) showed the same values at 20° and slightly improved towards low temperatures (−9% at −31°). Although a slightly better time resolution could be achieved, the overall trend of the time resolution at crystal lengths of 12 mm remained similar. As these results appear to be specific for this crystal geometry, a possible explanation might be related to effects of surface reflections or optical photon transport.

The FWTM of the time difference histogram shows a clear improvement towards shorter crystal lengths and ranges from ∼3 ns (20 mm, −31 °C) to ∼1.3 ns (3 mm, 20 °C). Interestingly,

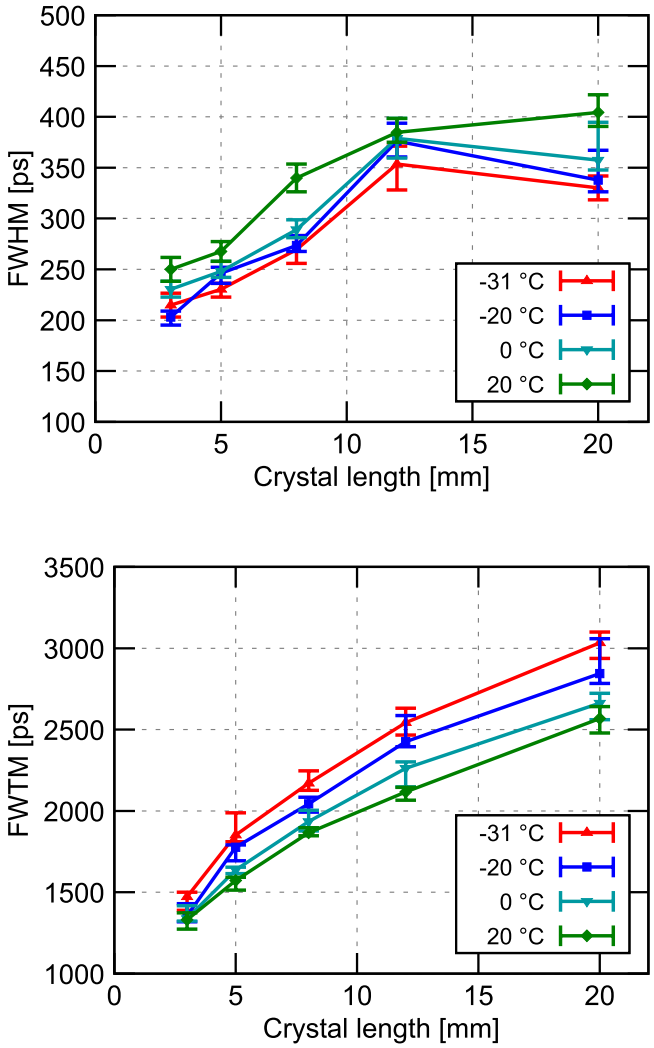

Figure 9. FWHM (top) and FWTM (bottom) of the time difference histograms measured with pairs of BGO crystals of different length and at different temperatures.

in comparison to the temperature dependence of the FWHM, the behavior of the FWTM is inversed, showing a significant improvement with increasing temperature. Apparently, the fast emission determining the FWHM has a different temperature dependence than the relatively slow emission of scintillation photons, which determines the FWTM. It is noted that the fast emission component is not expected to be dependent on temperature if it is linked to Cherenkov emission. Additionally, the variation of the FWTM seems to contradict the assumption that the time resolution improves with increasing light yield (figure 7). However, not only the light yield, but also the scintillation decay times are known to increase with decreasing temperature in BGO (Wolszczak 2014), which may explain the observed behavior.

Figure 10 shows the cumulative frequency distribution (CFD) of the time-difference histogram at 20 °C, for all 5 crystal lengths. Starting at a crystal length of 20 mm, the slope of the CFD clearly increases towards shorter crystal lengths. To describe each CFD quantitatively, the coincidence time windows t_p within which given percentages of the total number

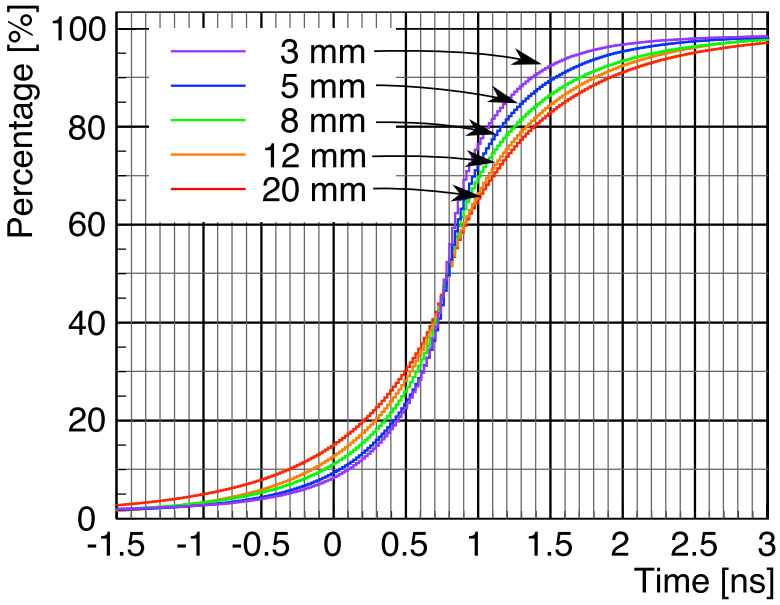

Figure 10. Cumulative frequency distribution (CFD) of the measured time-difference histogram at 20 °C, for five BGO crystals with different lengths.

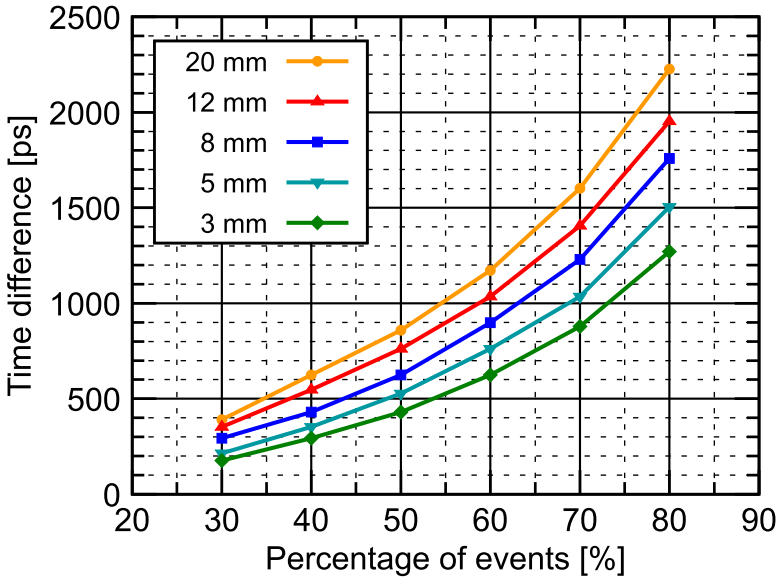

Figure 11. Coincidence time window within which a given percentage of the total number of coincidences occur.

of coincident events occur were determined, as described in section 2.4. Figure 11 shows the results, in the region between the 30th and 80th percentiles. Whereas the time windows $t_{30\%}$ within which 30% of all coincidences occur are below 500 ps for all crystal lengths, the values of $t_{80\%}$ reach from 1.3 ns (3 mm crystals) to 2.2 ns (20 mm crystals). For comparison, for a Gaussian distribution with a FWHM of 500 ps, $t_{30\%} = 164$ ps and a $t_{80\%} = 546$ ps.

4. Summary and conclusions

This work investigates the potential of using BGO as a hybrid scintillator / Cherenkov-radiator. Coincidence timing measurements were performed on BGO crystals with a cross-section of 3 mm × 3 mm and five different lengths ranging from 3 mm to 20 mm, coupled to DPC arrays. Non-Gaussian coincidence spectra with a FWHM of 200 ps were obtained with the 27 mm^3 BGO cubes, while FWHM values down to 330 ps were achieved with the 20 mm long crystals.

The luminescent response of BGO upon excitation by 511 keV annihilation photons was measured using a time-correlated single photon counting setup implemented on a DPC array, revealing a significant prompt luminescent component. We refer to this component as Cherenkov emission, but it is to be noted that the present data do not rule out the possibility that other fast luminescent mechanisms also play a role. Nevertheless, this work shows that the observed fast component enables unprecedented time resolutions in BGO.

The inversed temperature dependencies of the FWHM and FWTM of the time-difference histogram are further evidence that two different emission processes are present in BGO. Attributing the fast luminescent component to the Cherenkov effect implies that no variation of the emission with temperature is to be expected, so the observed improvement of the FWHM with decreasing temperature may primarily be due to the decreasing DPC dark count rate. On the other hand, the increase of the FWTM with decreasing temperature may be explained by the increasing scintillation decay time.

Interestingly, while the PDE of the DPC is not optimized for photon detection in the UV, the time resolutions in terms of the FWHM and FWTM of the time difference histograms that were obtained in this work to our knowledge are the best values reported for BGO to date. The use of a dSiPM with the combination of time-pickoff on the first detected photon and subsequent validation may be the main reason for these results: slightly improved CRT with crystals of double the volume (i.e. 27 mm^3) compared to Kwon *et al* (i.e. 12 mm^3) and ∼25% improved CRT for crystals of the same size (i.e. 3 mm × 3 mm × 20 mm) (Kwon *et al* 2016). In this context, it is to be noted that not only the length but also the cross-section of the crystal (3 mm × 3 mm in this work versus 2 mm × 2 mm for Kwon *et al*) is expected to influence the CRT (Gundacker *et al* 2016a).

In conclusion, the results presented in this work indicate that it may be feasible to combine event timing based on Cherenkov emission with energy discrimination based on scintillation in BGO, as a potential approach towards a cost-effective TOF-PET detector.

Acknowledgments

This work was partly funded by European Union's Horizon2020 Framework Programme, Marie Skłodowska-Curie action 659317 (PALADIN). See also http://fasttiming.weebly.com/.

References

Berger M J, Coursey J S, Zucker M A and Chang J 2005 *Estar, Pstar, and Astar: Computer Programs for Calculating Stopping-Power and Range Tables for Electrons, Protons, and Helium Ions (version 1.2.3)* (Gaithersburg, MD: NIST) (accessed 13 February 2016)

Bilevych Y *et al* 2016 Potential applications of electron emission membranes in medicine *Nucl. Instrum. Methods Phys. Res.* A **809** 171–4

Bollinger L M and Thomas G E 1961 Measurement of the time dependence of scintillation intensity by a delayed-coincidence method *Rev. Sci. Instrum.* **32** 1044–50

Borghi G, Tabacchini V, Bakker R and Schaart D 2016 TOF-PET imaging with sub-3 mm resolution and 215 ps coincidence resolving time using digital SiPM based monolithic scintillator detectors in a 70 cm diameter tomographic setup *J. Nucl. Med.* **57** 104

Brunner S E 2014 Fast single photon detection for scintillation and cherenkov applications using silicon photomultipliers *PhD Thesis* University of Technology, Vienna, Austria http://katalog.ub.tuwien.ac.at/AC11996520

Brunner S E, Ferri A, Gola A, Piemonte C and Schaart D R 2016a Comparative study on the time resolution of co-doped LSO:Ce, LYSO:Ce, LFS and LGSO:Ce *Talk at IEEE NSS/MIC (November 2016)*

Brunner S, Gruber L, Hirtl A, Suzuki K, Marton J and Schaart D 2016b A comprehensive characterization of the time resolution of the Philips digital photon counter *J. Instrum.* **11** P11004

Brunner S E, Gruber L, Marton J, Suzuki K and Hirtl A 2014 Studies on the cherenkov effect for improved time resolution of TOF-PET *IEEE Trans. Nucl. Sci.* **61** 443–7

Brunner S, Gruber L, Marton J, Suzuki K and Hirtl A 2013 New approaches for improvement of TOF-PET *Nucl. Instrum. Methods Phys. Res.* A **732** 560–3

Cates J W and Levin C S 2016 Advances in coincidence time resolution for PET *Phys. Med. Biol.* **61** 2255–64

Cho Z H, Farukhi M R, Diego S and Jolla L 1978 Analysis of a cylindrical hybrid positron camera with bismuth germanate (BGO scintillation crystals) *IEEE Trans. Nucl. Sci.* **NS-25** 952–63

Conti M 2011 Focus on time-of-flight PET: the benefits of improved time resolution *Eur. J. Nucl. Med. Mol. Imaging* **38** 1147–57

Derenzo S E, Budinger T F, Huesman R H, Cahoon J L and Vuletich T 1981 Imaging properties of a positron tomograph with 280 BGO crystals *IEEE Trans. Nucl. Sci.* **28** 81–9

Derenzo S E, Choong W S and Moses W W 2014 Fundamental limits of scintillation detector timing precision *Phys. Med. Biol.* **59** 3261–86

Derenzo S E, Weber M J, Moses W W and Dujardin C 2000 Measurements of the intrinsic rise times of common inorganic scintillators *IEEE Trans. Nucl. Sci.* **47** 860–4

Dolenec R, Korpar S, Krizan P, Pestotnik R, Stanovnik A and Verheyden R 2010 Time-of-flight measurements with Cherenkov photons produced by 511 keV photons in lead crystals *IEEE Nuclear Science Symp. and Medical Imaging Conf.* (IEEE) pp 280–4

Frach T 2012 Optimization of the digital silicon photomultiplier for Cherenkov light detection *J. Instrum.* **7** C01112

Frach T, Prescher G, Degenhardt C, de Gruyter R, Schmitz A and Ballizany R 2009 The digital silicon photomultiplier—Principle of operation and intrinsic detector performance *IEEE Nuclear Science Symp. Conf. Record (NSS/MIC)* pp 1959–65

Frach T, Prescher G, Degenhardt C and Zwaans B 2010 The digital silicon photomultiplier—system architecture and performance evaluation *IEEE Nuclear Science Symp. & Medical Imaging Conf.* (IEEE) pp 1722–7

Grant A M, Deller T W, Khalighi M M, Maramraju S H, Delso G and Levin C S 2016 NEMA NU 2-2012 performance studies for the SiPM-based ToF-PET component of the GE SIGNA PET/MR system *Med. Phys.* **43** 2334–43

Gundacker S, Acerbi D, Auffray E, Ferri A, Gola A, Nemallapudi M V, Paternoster G, Piemonte C and Lecoq P 2016a State of the art timing in TOF-PET detectors with LuAG, GAGG and L(Y)SO scintillators of various sizes coupled to FBK-SiPMs *J. Instrum.* **11** P08008

Gundacker S, Auffray E, Pauwels K and Lecoq P 2016b Measurement of intrinsic rise times for various L(Y)SO and LuAG scintillators with a general study of prompt photons to achieve 10 ps in TOF-PET *Phys. Med. Biol.* **61** 2802–37

Holl I, Lorenz E and Mageras G 1988 A measurement of the light yield of common inorganic scintillators *IEEE Trans. Nucl. Sci.* **35** 105–9

Humm J L, Rosenfeld A and Del Guerra A 2003 From PET detectors to PET scanners *Eur. J. Nucl. Med. Mol. Imaging* **30** 1574–97

Jelley J V 1958 *The Cerenkov Effect and its Applications* (London: Pergamon)

Jellison G E, Specht E D, Boatner L A, Singh D J and Melcher C L 2012 Spectroscopic refractive indices of monoclinic single crystal and ceramic lutetium oxyorthosilicate from 200 to 850 nm spectroscopic refractive indices of monoclinic single crystal and ceramic lutetium oxyorthosilicate from 200 to 850 nm *J. Appl. Phys.* **112** 063524

Karp J S, Surti S, Daube-Witherspoon M E and Muehllehner G 2008 Benefit of time-of-flight in PET: experimental and clinical results *J. Nucl. Med.* **49** 462–70

Korpar S, Dolenec R, Križan P, Pestotnik R and Stanovnik A 2011 Study of TOF PET using Cherenkov light *Nucl. Instrum. Methods Phys. Res.* A **654** 532–8

Kwon S I, Gola A, Ferri A, Piemonte C and Cherry S R 2016 Bismuth germanate coupled to near ultraviolet silicon photomultipliers for time-of-flight PET *Phys. Med. Biol.* **61** L38–47

Lecoq P, Annenkov A, Gektin A, Korzhik M and Pedrini C 2006 *Inorganic Scintillators for Detector Systems* (Berlin: Springer)

Lecoq P, Auffray E, Brunner S, Hillemanns H, Jarron P, Knapitsch A, Meyer T and Powolny F 2010 Factors influencing time resolution of scintillators and ways to improve them *IEEE Trans. Nucl. Sci.* **57** 2411–6

Liu Z, Gundacker S, Pizzichemi M, Ghezzi A, Auffray E, Lecoq P and Paganoni M 2016 In-depth study of single photon time resolution for the Philips digital silicon photomultiplier *J. Instrum.* **11** P06006

Mao R, Zhang L and Zhu R Y 2007 Optical and scintillation properties of inorganic scintillators in high energy physics *IEEE Nuclear Science Symp. Conf. Record* vol 3 pp 2285–91

Melcher C and Schweitzer J 1992 A promising new scintillator: cerium-doped lutetium oxyorthosilicate *Nucl. Instrum. Methods Phys. Res.* A **314** 212–4

Miller M 2016 Philips Vereos white paper www.digitalpetlearningcenter.philips.com/downloads/452299119831_Vereos_Perf_WP.pdf

Miller M, Zhang J, Binzel K, Griesmer J, Laurence T, Narayanan M, Natarajamani D, Wang S and Knopp M 2015 Characterization of the vereos digital photon counting PET system *J. Nucl. Med.* **56** 434

Miyata M, Tomita H, Watanabe K, Kawarabayashi J and Iguchi T 2006 Development of TOF-PET using Cherenkov radiation *J. Nucl. Sci. Tech.* **43** 339–43

Moses W W 2007 Recent advances and future advances in time-of-flight PET *Nucl. Instrum. Methods Phys. Res.* A **580** 919–24

Moszyński M, Gresset C, Vacher J and Odru R 1981 Timing properties of BGO scintillator *Nucl. Instrum. Methods Phys. Res.* **188** 403–9

Nemallapudi M V, Gundacker S, Lecoq P, Auffray E, Ferri A, Gola A and Piemonte C 2015 Sub-100 ps coincidence time resolution for positron emission tomography with LSO:Ce codoped with Ca *Phys. Med. Biol.* **60** 4635–49

Nitsche R 1965 Crystal growth and electro-optic effect of bismuth germanate, Bi4 (GeO4)3 *J. Appl. Phys.* **36** 2358

Ooba T, Fukushima T, Kawai H, Konishi M, Nakayama H, Tabata M, Adachi I, Nishida S, Kishimoto H and Yokogawa H 2004 Proposal of Cherenkov TOFPET with silica aerogel *IEEE Nuclear Science Symp. Conf. Record* vol 6 pp 3781–4

Philips Digital Photon Counting, Aachen, Germany 2015 DPC3200 leaflet www.digitalphotoncounting.com (accessed: January 2017)

Schaart D R, Charbon E, Frach T and Schulz V 2015 Advances in digital SiPMs and their application in biomedical imaging *Nucl. Instrum. Methods Phys. Res.* A **809** 31–52

Schaart D R, Seifert S, Vinke R, van Dam H T, Dendooven P, Löhner H and Beekman F J 2010 LaBr(3):Ce and SiPMs for time-of-flight PET: achieving 100 ps coincidence resolving time *Phys. Med. Biol.* **55** N179–89

Schug D, Wehner J, Dueppenbecker P M, Weissler B, Gebhardt P, Goldschmidt B, Solf T, Kiessling F and Schulz V 2015 ToF performance evaluation of PET modules with digital silicon photomultiplier technology during MR operation *IEEE Trans. Nucl. Sci.* **62** 658–63

Schulze R 2015 Tile-TEK Manual v1.00 Philips Digital Photon Counting; Tile-TEK - User Manual v1.03; published 2016–10

Seifert S, Steenbergen J H L, van Dam H T and Schaart D R 2012 Accurate measurement of the rise and decay times of fast scintillators with solid state photon counters *J. Instrum.* **7** P09004

Somlai-Schweiger I and Ziegler S I 2015 CHERENCUBE: concept definition and implementation challenges of a Cherenkov-based detector block for PET *Med. Phys.* **42** 1825–35

Spurrier M A, Szupryczynski P, Yang K, Carey A A and Melcher C L 2008 Effects of Ca^{2+} co-doping on the scintillation properties of LSO:Ce *IEEE Trans. Nucl. Sci.* **55** 1178–82

Surti S, Kuhn A, Werner M E, Perkins A E, Kolthammer J and Karp J S 2007 Performance of Philips Gemini TF PET/CT scanner with special consideration for its time-of-flight imaging capabilities *J. Nucl. Med.* **48** 471–80 (PMID: 17332626)

Tabacchini V, Westerwoudt V, Borghi G, Seifert S and Schaart D R 2014 Probabilities of triggering and validation in a digital silicon photomultiplier *J. Instrum.* **9** P06016

Thompson C J, Yamamoto Y L and Meyer E 1979 Positome II: a high efficiency positron imaging device for dynamic brain studies *IEEE Trans. Nucl. Sci.* **26** 583–9

Vandenberghe S, Mikhaylova E, D'Hoe E, Mollet P and Karp J S 2016 Recent developments in time-of-flight PET *EJNMMI Phys.* **3** 3

Weele D N, Schaart D R, Member S and Dorenbos P 2015 Comparative study of co-doped and non co-doped LSO:Ce and LYSO:Ce scintillators for TOF-PET *IEEE Trans. Nucl. Sci.* **62** 727–31

Williams P A, Rose A H, Lee K S, Conrad D C, Day G W and Hale P D 1996 Optical, thermo-optic, electro-optic, and photoelastic properties of bismuth germanate ($Bi_4Ge_3O_{12}$) *Appl. Opt.* **35** 3562–9

Wolszczak W 2014 Depth of interaction determination with temperature gradient function in continuous bismuth germanate oxide (BGO) crystal *Bio-Algorithms Med-Syst.* **10** 65–70

Wolszczak W, Moszynski M, Szczesniak T, Grodzicka M and Kacperski K 2014 Temperature properties of scintillators for PET detectors: a comparative study *2014 IEEE Nuclear Science Symp. and Med ical Imaging Conf.* vol 137 pp 1–4